Imaging Metastasis Using an Integrin-Targeting Chain-Shaped Nanoparticle

Pubudu M. Peiris,[†,‡,§] Randall Toy,[†,§] Elizabeth Doolittle,[†,§] Jenna Pansky,[†,§] Aaron Abramowski,[†,§] Morgan Tam,[†,§] Peter Vicente,[†,§] Emily Tran,[†,§] Elliott Hayden,[†,§] Andrew Camann,[†,§] Aaron Mayer,[†,§] Bernadette O. Erokwu,[‡,§] Zachary Berman,[‡,§] David Wilson,[†,§,⊥] Harihara Baskaran,[⊥,∥] Chris A. Flask,[†,‡,§,⊥] Ruth A. Keri,[⊥,¶] and Efstathios Karathanasis[†,‡,§,⊥,*]

[†]Department of Biomedical Engineering, [‡]Department of Radiology, [§]Case Center for Imaging Research, [⊥]Case Comprehensive Cancer Center, [∥]Department of Chemical Engineering, and [¶]Department of Pharmacology, Case Western Reserve University, Cleveland, Ohio

ABSTRACT

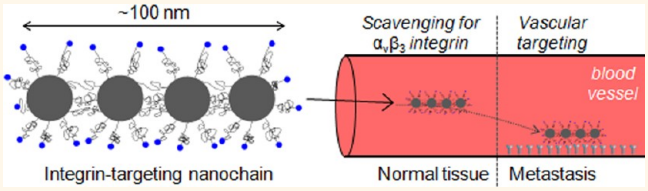

While the enhanced permeability and retention effect may promote the preferential accumulation of nanoparticles into well-vascularized primary tumors, it is ineffective in the case of metastases hidden within a large population of normal cells. Due to their small size, high dispersion to organs, and low vascularization, metastatic tumors are less accessible to targeted nanoparticles. To tackle these challenges, we designed a nanoparticle for vascular targeting based on an $\alpha_v\beta_3$ integrin-targeted nanochain particle composed of four iron oxide nanospheres chemically linked in a linear assembly. The chain-shaped nanoparticles enabled enhanced "sensing" of the tumor-associated remodeling of the vascular bed, offering increased likelihood of specific recognition of metastatic tumors. Compared to spherical nanoparticles, the chain-shaped nanoparticles resulted in superior targeting of $\alpha_v\beta_3$ integrin due to geometrically enhanced multivalent docking. We performed multimodal *in vivo* imaging (fluorescence molecular tomography and magnetic resonance imaging) in a non-invasive and quantitative manner, which showed that the nanoparticles targeted metastases in the liver and lungs with high specificity in a highly aggressive breast tumor model in mice.

KEYWORDS: iron oxide nanoparticle · nanochain · metastasis · integrin targeting · magnetic resonance imaging

While conventional small molecule therapeutics are distributed within cancer and healthy tissues in a nonspecific manner, nanoparticle delivery systems have been developed to exploit a feature of the tumor microenvironment, the so-called "enhanced permeability and retention" (EPR) effect.[1] Due to the tumor's leaky vasculature, the intratumoral accumulation of nanoparticles is high relative to normal tissues.[2−5] While the EPR strategy may be effective in large, well-vascularized tumors, it is very ineffective in metastatic disease, which presents small clusters of malignant cells within variable tissue types.[6] Notably, the 5 year survival rate of breast cancer patients sharply decreases from 98% in cases with localized primary lesions to 23% in cases of distant metastases.[7] The vast majority of cancer deaths are due to metastatic disease; hence, it is essential to design nanotechnology-based agents that can successfully target metastatic tumors.

Targeting a metastatic lesion within a large population of normal cells presents a unique challenge. Metastases present biobarriers due to their smaller size, higher dispersion to organs, and lower vascularization than primary tumors, making them less accessible to molecular or nanoparticle agents. However, metastatic lesions can upregulate specific cell-surface molecules and secreted factors that differ from the rest of its host organ. If the appropriate chemical specificity is selected, targeted nanoparticles could provide a unique opportunity to home imaging and therapeutic compounds to metastases. Several conceptual and experimental theories of metastatic cancer have been recently explored that may be exploited for nanoparticle targeting.[8,9] For example, β_3 integrins have shown to play a key role in migration, invasion, and metastasis.[10−16] It has been shown that the metastatic site transitions from selectin-dependent tumor cell rolling on the endothelium to firm attachment that is mediated primarily by $\alpha_v\beta_3$ integrins.[10,12] Thus, $\alpha_v\beta_3$ integrin is a very attractive target.[17] While various studies have used integrin-binding peptides

* Address correspondence to stathis@case.edu.

Received for review June 10, 2012 and accepted September 19, 2012.

Published online September 24, 2012
10.1021/nn303833p

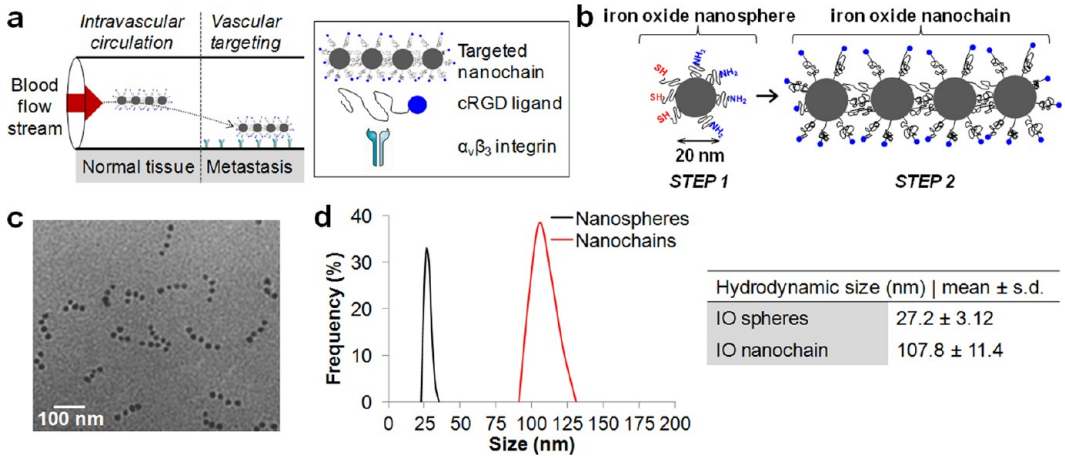

Figure 1. Characterization of the RGD-NC nanoparticles. (a) Illustration of the models for the successful delivery of RGD-NC nanoparticles to metastasis *via* vascular targeting. (b) Diagram of the RGD-NC nanoparticle and its constituent components. (c) TEM image of RGD-NC nanoparticles predominantly composed of four IO spheres. (d) Size distribution of the parent IO nanospheres and RGD-NC nanoparticles obtained by DLS measurements.

to target nanoparticles to tumors,[16−24] the preclinical development of these systems has focused predominantly on tumors at the primary site. Taking under consideration the microenvironment of metastatic tumors, a targeted nanoparticle capable of "sensing" the metastasis-associated remodeling of the vascular bed may offer an increased likelihood of specific recognition of tumors. In this work, we report the design of a nanoparticle-targeting $\alpha_v\beta_3$ integrin for non-invasive imaging of metastasis (Figure 1a). Specifically, we selected the cyclic tripeptide arginine−glycine−aspartic acid (cRGD) peptide as the ligand for vascular targeting of the nanoparticle to metastases.[19,23,24] We exploited the nanochain technology to fabricate a chain-shaped nanoparticle composed of four iron oxide (IO) nanospheres chemically linked into a linear assembly (Figure 1b).[25,26] The high aspect ratio and flexibility of the nanoparticle substantially increased its chances to successfully seek metastatic lesions due to geometrically enhanced multivalent docking[27] to the vasculature of metastases. Due to this high avidity and increased magnetic relaxivity of the nanochain particles,[26] we were able to detect metastatic lesions in an aggressive breast tumor model in mice using small animal fluorescence molecular tomography (FMT) and magnetic resonance imaging (MRI). This approach should also be useful for selective targeting of therapeutic agents to metastases.

RESULTS

Fabrication and Characterization of the Integrin-Targeted Nanoparticle. Fabrication of the integrin-targeted nanoparticle (termed RGD-NC) was based on the nanochain technology,[26] which is a two-step approach using solid-phase chemistry. In the first step, amine-functionalized IO nanospheres were attached on a solid support *via* a cross-linker containing a disulfide bridge. Liberation of the nanosphere using thiolytic cleavage created thiols on the portion of the particle's surface that interacted with the solid support, resulting in a particle with two faces, one displaying only amines and the other only thiols. Therefore, we were able to topologically control the conversion of amines on the surface of the IO nanospheres into thiols, resulting in a particle with asymmetric surface chemistry. In the second step, employing solid-phase chemistry and step-by-step addition of particles, the two unique faces on the same IO nanosphere served as fittings to assemble them into linear nanochains (Figure 1b). The nanochains were analyzed *via* visual inspection of multiple TEM images. As shown in Figure 1c, the nanochains were synthesized in a highly controlled manner. Most of the nanochains are linear and consist of four IO spheres with the overall geometrical dimensions of the particle being about 100 × 20 nm (length × width). To evaluate the robustness of the nanochain synthesis, the number of IO nanospheres per nanochain was measured in TEM images. While 6% of the total particles in the suspension were the parent (unbound) IO spheres, the majority of the particles (72%) comprised nanochains with four IO spheres (12 and 10% were nanochains with 3 or 5 IO spheres, respectively). As shown in Figure 1d, the hydrodynamic size of the particle and its constituent IO spheres, as measured by dynamic light scattering (DLS), verified the TEM images. It should be noted that DLS measured the effective hydrodynamic diameter based on the diffusion of the particles. Since the hydrodynamic diameter measured by DLS does not correspond to the geometrical size of nonspherical particles, we relied on visual analysis of TEM images to measure the exact dimensions of the nanochain. Detailed characterization of the nanochain particles is reported in a previous publication.[26]

The cyclo (Arg-Gly-Asp-D-Phe-Cys) or c(RGDfC) was conjugated onto the distal end of the PEG-NH_2 on the

particle's surface. While Figure 1c shows the nanochain after modification with the RGD peptide, a TEM image of the nanochain prior to modification is shown in Figure S1 in Supporting Information. In addition to conjugation of the peptide, the nanochain particles were labeled with an NIR fluorophore (VivoTag 680) to be detectable by fluorescence imaging. To evaluate the effect of the geometry on the magnetization, we compared the r_2 relaxivity of the RGD-NC particle to that of its parent IO nanospheres by measuring the transverse (R_2) relaxation rates at 1.4 T. The r_2 value of the RGD-NC particle was 121 s^{-1} mM^{-1}, which was 2.1-fold higher than that of its constituent IO spheres. Detection of metastasis *via* receptor-mediated targeting depends on the generation of signal from each nanoparticle. Thus, we calculated the T_2 relaxivity on a per nanoparticle basis, which was 8.4 times higher for the RGD-NC particle compared to its constituent IO nanospheres.

Targeting of the RGD-NC nanoparticles to integrin-expressing endothelial cells was evaluated *in vitro* under static and flow conditions. Bovine aortic endothelial cells (BAEC) were treated with TNF-α to induce expression of $\alpha_v\beta_3$ integrins[28] and then incubated with an excess of the RGD-NC nanoparticles for different periods of time. As shown in Figure S2a in Supporting Information, the time course of the nanoparticle uptake by the cells showed that the binding of the nanoparticles occurs rapidly during the first 30 min of incubation. In a similar manner, we evaluated the cellular uptake by 4T1 cells indicating that the integrin-targeting RGD-NC nanoparticles were also able to target the cancer cells (Figure S2b). This is significant because the metastatic 4T1 cells colonize the endothelium as we show later in the histological evaluation.

Successful vascular targeting requires that a nanoparticle can escape the blood flow and drift toward the blood vessel walls (*e.g.*, high margination), followed by strong attachment to the targeting site offsetting the blood flow forces that tend to detach the particle (*e.g.*, high avidity). Since both margination and avidity of nanoparticles in circulation strongly depend on the geometry of the nanoparticle,[27,29−32] we measured the margination rates and avidity of the nanochains in microvasculature constructs under flow conditions using our previously established *in vitro* method.[32] The experiments were conducted in a microfluidic flow network setup (Figure S2c in Supporting Information) because channel dimensions and infusion rates can be accurately controlled removing the complexity of *in vivo* studies. First, TEM images of the nanochain suspension in cell culture media were obtained after the nanoparticles were flowed in the microchannel for 20 min at 50 μL/min, indicating that the particles maintain their structural integrity under flow conditions (Figure S2c). To separate margination from targeting avidity, we initially evaluated the margination of nontargeted nanochains. To avoid undesirable specific binding events, the channel was coated with fibronectin, which captures marginating particles in a broad nonspecific manner.[32] At a flow rate of 50 μL/min, which is in the range of expected blood flow in tumor microcirculation,[33] the nanochain exhibited 2.3-fold higher margination than the IO sphere (Figure S2d). Targeting avidity of the RGD-NC particle was also assessed under flow using the microfluidic device coated with TNF-α-treated BAEC cells. RGD-NC nanoparticles and RGD-targeted nanospheres displayed a biphasic behavior comprising an initial rapid attachment phase followed by a slower attachment rate (Figure S2e). Importantly, after 5 and 20 min, the RGD-NC nanoparticles achieved 9.5- and 2.9-fold higher attachment compared to their spherical counterparts. We should note that the ligand density on the surface of nanospheres or nanochains was the same, being about 25 RGD peptides per sphere. Thus, the total number of RGD peptides on a nanochain was about 100.

Targeting the Primary Tumor. We used the orthotopic 4T1 mammary tumor model in mice to assess the potential utility of RGD-NC nanoparticles for detection of primary tumors and metastases. The 4T1 cell line is one of the few breast cancer models that efficiently metastasizes to sites and organs similar to that observed in the human disease.[34,35] Previous studies[34] have shown that growth of cells at the primary site displays a biphasic behavior: (1) the primary tumor rapidly grows in the first 2 weeks after inoculation of tumor cells in the mammary fat pad; (2) the tumor shrinks in the next 2 weeks due to infiltration of leukocytes and extensive necrosis; (3) during the fifth week, the tumor grows again with metastases occurring primarily in the liver, spleen, and lungs.

Initially, we compared the RGD-NC particles to RGD-targeted IO nanospheres (RGD-NS) and their nontargeted variants in their ability to target the primary tumor (early stage: week 2 after tumor inoculation). All formulations were administered at a dose containing an equal number of particles per kilogram of body weight (*i.e.*, 1.3×10^{14} particles/kg b.w. corresponding to 0.21 and 0.87 mg Fe/kg b.w. for the IO nanospheres and nanochains, respectively). Using fluorescence molecular tomography (FMT) imaging, we non-invasively and quantitatively monitored the time-dependent intratumoral accumulation of the various particles (equal number of NIR fluorophores/particle). Figure 2a shows representative FMT images that were taken 30 min after systemic administration of the formulations. Due to their enhanced multivalent docking, the RGD-NC nanoparticles substantially outperformed the targeted nanospheres. As expected, the nontargeted nanochains exhibited slow accumulation into the primary tumor primarily due to the EPR effect. As shown in Figure 2b, the intratumoral accumulation of the

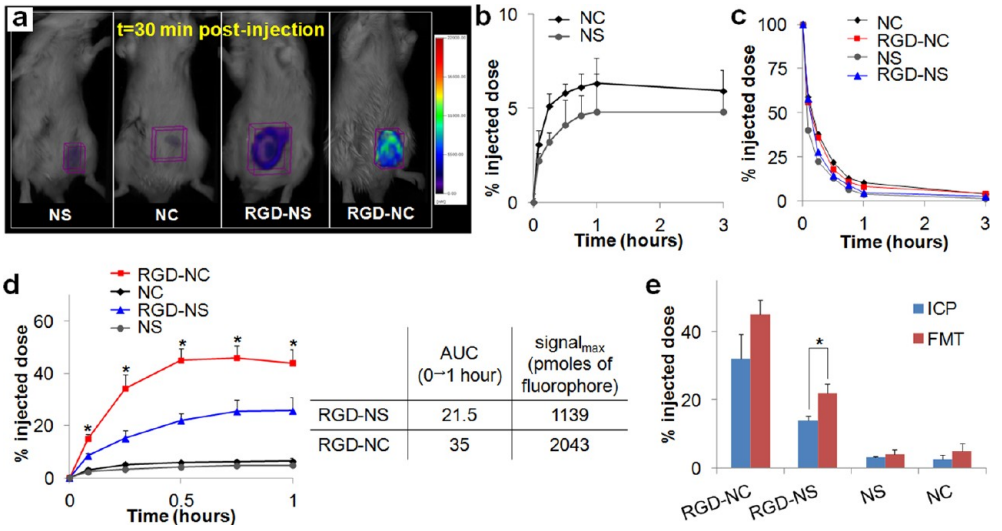

	AUC (0→1 hour)	signal$_{max}$ (pmoles of fluorophore)
RGD-NS	21.5	1139
RGD-NC	35	2043

Figure 2. Evaluation of the ability of the RGD-NC nanoparticles to target primary 4T1 tumors (early stage tumor model: week 2 after tumor inoculation). (a) FMT images show the accumulation of RGD-targeted and nontargeted IO spheres and nanochains in primary tumors at 30 min post-injection (dose: equal number of particles per kg of body weight). The nanoparticles of each formulation exhibited the same fluorescence signal per particle. (b) Quantification of the time course of accumulation of the nontargeted nanospheres and nanochains in the tumor due to the EPR effect. (c) Time course of the amount of nanoparticles in the heart as a measure of the blood residence time of each formulation. (d) Comparison of the intratumoral accumulation of targeted nanochains and nanospheres and their nontargeted variants in the first 1 h after administration. It should be noted the range of *x*- and *y*-axes are different between panels b and c. While the RGD-targeted IO spheres exhibited higher tumor accumulation than the nontargeted formulations, they were substantially outperformed by the RGD-NC nanoparticles (data presented as mean ± standard deviation). (e) Primary tumors of animals injected with NS, NC, RGD-NS, or RGD-NC were perfused, excised, and weighed 30 min after administration. After digestion of the tissues, the iron concentration was measured using inductively coupled plasma optical emission spectroscopy (ICP-OES). Control animals were used to correct for background levels of endogenous iron. In the FMT and ICP measurements, data points marked with asterisks are statistically significant relative to all groups (n = 6 animals per formulation; *P < 0.05).

nontargeted nanochains was about 5.9% of the injected dose at t = 3 h post-injection. We should emphasize that the nanochains and nanospheres were not fully covered with the polyethylene glycol (PEG) coating. This is evident by the blood residence time of the nanoparticles shown in Figure 2c (blood $t_{1/2}$ ~ 20 min; measured in the heart) since the circulation time of nanoparticles depends on the degree of PEG shielding.[36,37] Our objective was to detect a signal from the RGD-NC particles targeting integrins on the tumor-associated vascular bed with no interference from the signal in the vascular site. If the particles are bound to the tumor vasculature, the time point of maximum signal from the tumor site should coincide with low concentration of the nanoparticles in the bloodstream. Figure 2d shows the time course of the fluorescent signal in the tumor for each formulation. Indeed, the RGD-NC-injected animals displayed maximum signal in the tumor in the 30−60 min time window, while the nanoparticles were almost depleted from the bloodstream. Most importantly, at t = 45 min after injection, the tumor accumulation of RGD-NC was 8-fold higher than their nontargeted variant. At that time point, vascular targeting *via* the RGD peptide resulted in more than 40% of the administered nanochains being localized in the primary tumor. Quantitative measures of the intratumoral deposition of each particle (*i.e.*, area under the curve and maximum signal denoted as AUC$^{0\rightarrow1h}$ and signal$_{max}$, respectively) are shown in the table of Figure 2d. In general, these data are consistent with the *in vitro* targeting experiments showing that the RGD-NC particles achieved significantly higher vascular targeting at an earlier time point. At later time points, low levels of agent remained in circulation 24 h after administration. Mostly, the agent was found in the liver and spleen with less that 5% of the injected dose being in the heart or kidney.

To validate the *in vivo* FMT-based measurements, the iron concentration of the primary tumors of animals injected with the formulations was directly measured *ex vivo* using ICP-OES (inductively coupled plasma optical emission spectroscopy). Animals injected with saline were used for correction of the background levels of iron in the tumor tissue. Figure 2e shows the intratumoral iron content 30 min after injection of targeted and nontargeted nanochains and nanospheres, verifying the patterns observed with FMT imaging. While the FMT measurements slightly overestimated the intratumoral concentration of the nanoparticles compared to the ICP measurement, the only statistically different condition was the case of RGD-NS. Notably, ICP confirmed that more than 35% of the administered RGD-NC particle accumulated in the tumor within 30 min after administration.

Targeting Metastases. To evaluate the ability of the RGD-NC particles to target metastasis, we used mice

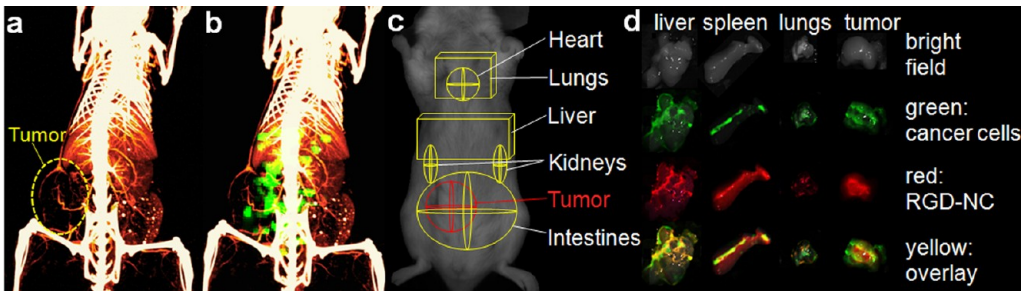

Figure 3. Imaging of metastases. (a) Micromorphological imaging of normal and tumor vasculature at 99 μm resolution of a metastatic 4T1 tumor (week 5) using a Siemens Inveon micro-CT and a liposome-based iodinated contrast agent. (b) Co-registration of the micro-CT image with the FMT image of the same animal injected with the RGD-NC nanoparticles. (c) ROIs indicate the location of the tumor and different organs as obtained from previously published work.[41] (d) Using a CRi Maestro fluorescence imaging system, *ex vivo* imaging of organs indicates the colocalization of RGD-NC particles and 4T1 metastatic cells expressing GFP.

with a late-stage 4T1 tumor (week 5 after tumor inoculation). We performed whole body angiography at 99 μm resolution using a micro-CT system (Siemens Inveon) and a liposomal imaging agent encapsulating a high cargo of an iodinated contrast agent.[38−40] Consistent with previous reports,[34] Figure 3a indicates that the primary tumor of this animal model at a late stage presented a necrotic core with little internal vascularization and a vascularized periphery. The same animal was systemically injected with RGD-NC nanoparticles tagged with an NIR fluorophore and imaged with the FMT system. Three-dimensional-rendered volumes of the micro-CT angiogram and the FMT image (45 min post-injection) were co-registered using a script-based software (in MATLAB) and the interactive visualization software Amira (Figure 3b). The accumulation of the RGD-NC particles in the primary tumor site was primarily observed in the location of blood vessels, which is consistent with the expression of integrins due to tumor-associated angiogenesis. Importantly, significant fluorescence signal was detected in other organs away from the primary tumor site. On the basis of previously published work,[41] regions of interest (ROIs) were selected in the FMT image to indicate the location of major organs (Figure 3c), showing that the RGD-NC nanoparticles accumulated in other organs besides the primary tumor (*e.g.*, liver and lungs). To confirm the colocalization of RGD-NC particles and metastatic tumors, organs were imaged *ex vivo* using a CRi Maestro fluorescence imaging system because the 4T1 cell line was engineered to stably express green fluorescent protein (GFP). We should note that the fluorescence signals from GFP and the nanoparticle's NIR tag do not overlap. Figure 3d confirms the presence of metastatic tumors in the liver, spleen, and lungs (other organs are not shown because no signal from GFP was detected). Grossly, the metastatic tumors appeared as white nodules in bright-field imaging, compared to the darker liver parenchyma. More importantly, the signals from metastatic cancer cells (green) and RGD-NC particles (red) overlaid significantly (yellow), indicating the localization of the nanoparticles in metastatic lesions.

The efficacy of the RGD-NC nanoparticles to target metastatic tumors was quantitatively evaluated in a group of mice harboring metastatic 4T1 tumors ($n = 6$) using FMT imaging. Figure 4a shows representative images of a normal mouse (top row) and a mouse with metastases (bottom row) imaged with the FMT system at $t = 30$ min after injection of RGD-NC. The relatively low signal in the lungs of normal animals ($n = 6$) suggested the presence of the agent primarily in the bloodstream. Since RGD-NC nanoparticles are primarily cleared by liver Kupffer cells (and splenic macrophages), the liver of the same animals exhibited relatively appreciable signal compared to the lungs. On the other hand, FMT imaging of mice with late-stage 4T1 tumors showed significant accumulation of RGD-NC primarily in regions of the liver and lungs. Using the designated ROIs for each organ (as shown in Figure 3c), we measured the concentration of RGD-NC in locations of those organs displaying significantly enhanced signal (*i.e.*, hot spots). In each "metastatic" animal, we identified 1−3 hot spots in the liver and lungs designated as ROI-1 and ROI-2 in Figure 4a, respectively. The quantitative analysis shown in Figure 4b revealed a significant concentration of the agent in these hot spots. More importantly, these hot spots displayed a 15- and 7.2-fold increase of signal compared to the background signal in healthy liver and lungs.

Imaging of Metastasis Using MRI. To detect metastases using a clinically relevant imaging modality, we performed imaging with MRI. Figure 5 shows representative coronal T_2-weighted images of healthy mice ($n = 3$) and metastatic 4T1 mice ($n = 2$) obtained using a 9.4 T MRI before and after administration of the RGD-NC nanoparticles (at a dose of 1.74 mg Fe/kg b.w.). This dose is substantially lower than the typical dose of IO nanoparticles used in MR imaging studies (*e.g.*, 10 mg Fe/kg).[42] MR images were acquired a few minutes prior to injection of the agent and 15, 30, 45, and 60 min after

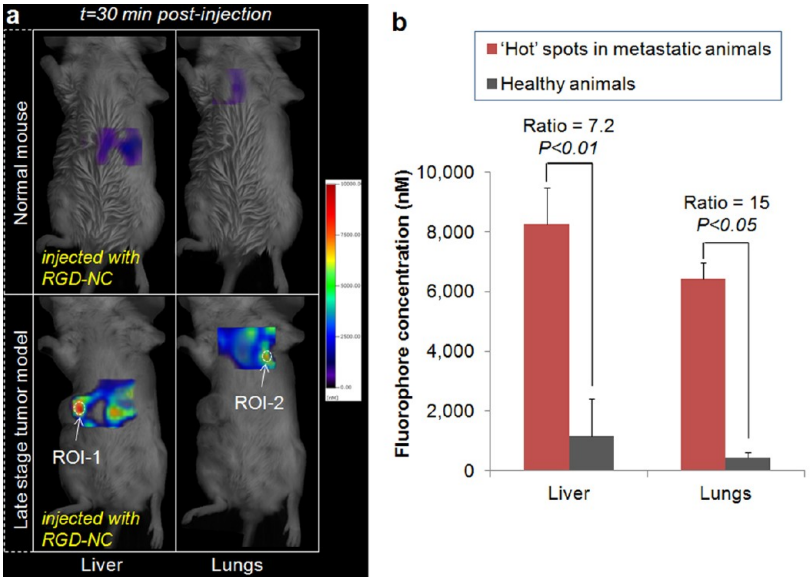

Figure 4. Evaluation of the ability of the RGD-NC nanoparticles to target metastatic 4T1 tumors (late-stage tumor model: week 5 after tumor inoculation). (a) Representative FMT images show the accumulation of the RGD-NC particles in the liver and lungs of healthy and metastasis-bearing mice at 30 min post-injection. In the animal with metastases, hot spots with a significantly elevated concentration of the particles are indicated in the liver and spleen as ROI-1 and ROI-2, respectively. (b) Quantification of the fluorescence signal obtained from the FMT images of a group of healthy mice and a group of metastatic mice 30 min after injection of RGD-NC particles (data presented as mean ± standard deviation). The signal of the hot spots in the lungs and liver of the metastatic group was compared to the average signal of these organs in the healthy group ($n = 6$ animals per group).

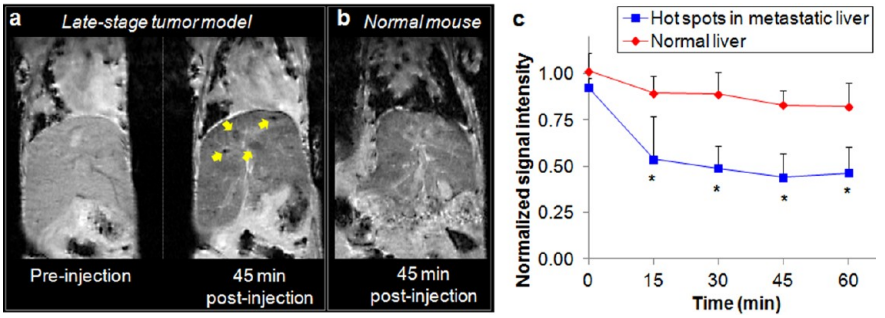

Figure 5. Representative *in vivo* MR images of the liver in normal and metastatic mice using a 9.4 T MRI. (a) Coronal T_2-weighted images of the liver of a metastatic mouse before and 45 min after injection of the RGD-NC nanoparticles. In the 45 min post-injection image, the yellow arrows show micrometastases of about 0.5 mm in size with increased contrast enhancement. (b) Coronal T_2-weighted images of the liver of a normal mouse 45 min after injection of the RGD-NC nanoparticles. (c) Time course of the MR signal intensity in the liver hot spots was quantitatively evaluated. The absolute MR signal intensity in the metastatic lesions and the healthy liver was measured in manually drawn ROIs. The signal intensity in the hot spots or the entire healthy liver was normalized to the signal of an adjacent muscle (scale: 0−1). Since lower values indicate greater contrast in T_2 images, normalized intensity values of 0 and 1 correspond to maximum and minimum contrast, respectively, compared to the precontrast intensity values (data presented as mean ± standard deviation; $n = 3$; each metastatic animal exhibited 2−4 hot spots; $^*P < 0.05$).

injection. The scanning parameters in the pre- and post-injection images were identical. Figure 5a compares the pre-injection and 45 min post-injection images of the liver in a metastatic animal. The uptake of the agent by the macrophages in the liver generated an appreciable negative contrast. However, targeting of the RGD-NC nanoparticles to metastatic lesions achieved a significantly higher negative contrast (yellow arrows in Figure 5a) that "overshadowed" the background contrast in the liver. As described in the next section, histological evaluation of the liver confirms the accumulation of the agent in metastatic tumors. Figure 5b shows a 45 min post-injection image of a healthy liver demonstrating that the uptake of the agent in the liver generated homogeneous contrast with no "hot" spots. To quantitatively evaluate the ability of the RGD-NC nanoparticles to target metastasis, the absolute MR signal intensity in the metastatic lesions and the healthy liver was measured using manually drawn regions of interest. Figure 5c shows that the time course of the signal intensity in the hot spots or the entire healthy liver (normalized to the signal of an adjacent muscle; scale: 0−1). Lower values indicate greater contrast in T_2 images, and a

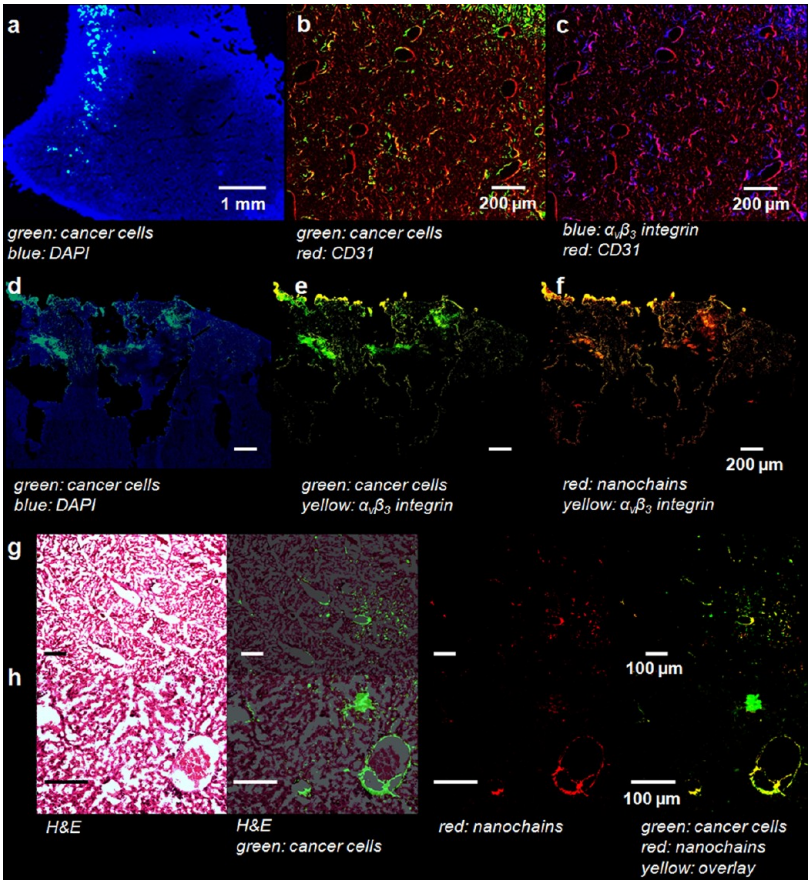

Figure 6. Histological evaluation of the microdistribution of the RGD-NC nanoparticles in the liver of animal with metastatic tumors. (a) Fluorescence image of a histological section of the left lobe of the liver (5× magnification; blue, nuclear stain (DAPI); green, 4T1 cancer cells (GFP)). Images of entire histological sections of the organs were obtained using the automated tiling function of the microscope. (b,c) Location of metastatic cancer cells is shown with respect to endothelial cells and expression of $\alpha_v\beta_3$ integrin in the same histological section (10× magnification; green, 4T1 cancer cells; red, endothelial cells; blue, $\alpha_v\beta_3$ integrin). (d−f) RGD-NC particles accumulated in locations of 4T1 cells that expressed $\alpha_v\beta_3$ integrin (10× magnification; blue, DAPI; green, 4T1 cancer cells; yellow, $\alpha_v\beta_3$ integrin; red, RGD-NC). (g,h) Fluorescence and bright-field microscopy was performed on histological sections stained with hematoxylin−eosin, showing the colocalization of RGD-NC and cancer cells and their relative anatomical location in the liver (5× and 10× magnification in g and h; green, 4T1 cancer cells; red, RGD-NC; yellow, overlay).

normalized intensity value of 1 corresponds to no contrast compared to the precontrast image. The preinjection values for both the normal liver and the hot spots in the metastatic liver were fairly similar and close to 1. As expected, due to clearance of the particles by the liver, injection of RGD-NC resulted in contrast enhancement in the healthy liver with an intensity value of 0.83. However, the metastatic lesions exhibited a normalized signal intensity value of ~0.44 in the post-injection images, indicating significantly higher contrast compared to the post-injection background signal of the healthy or uninvolved regions of the metastatic liver. It is important to note that this contrast may be further improved by optimization of the MR imaging parameters or by quantifying the T_2* relaxation values directly.

Histological Evaluation. After the last *in vivo* imaging session, tissues were collected and histological analysis was performed to confirm the localization of the RGD-NC nanoparticles in metastatic tumors. We histologically examined the animals used in the *in vivo* imaging studies, verifying the presence of RGD-NC nanoparticles in the majority of metastases. We evaluated the location of the metastatic cancer cells with respect to blood vessels and the associated expression of $\alpha_v\beta_3$ integrin. Using fluorescence microscopy, we verified that metastatic tumors were present in the liver and lungs of all the animals at a late stage (week 5 after tumor inoculation). Images of entire histological sections of the organs were obtained at a low magnification (5×) using the automated tiling function of the microscope. A representative image of the left lobe of liver is shown in Figure 6a, displaying the presence of clusters of metastatic cells (green) dispersed in the liver parenchyma. Imaging at higher magnification showed that the metastatic cancer cells were localized primarily on the endothelial walls (Figure 6b). Furthermore, these were exactly the locations that exhibited "remodeling" as indicated by the overexpression of $\alpha_v\beta_3$ integrins (Figure 6c). We should note that negligible

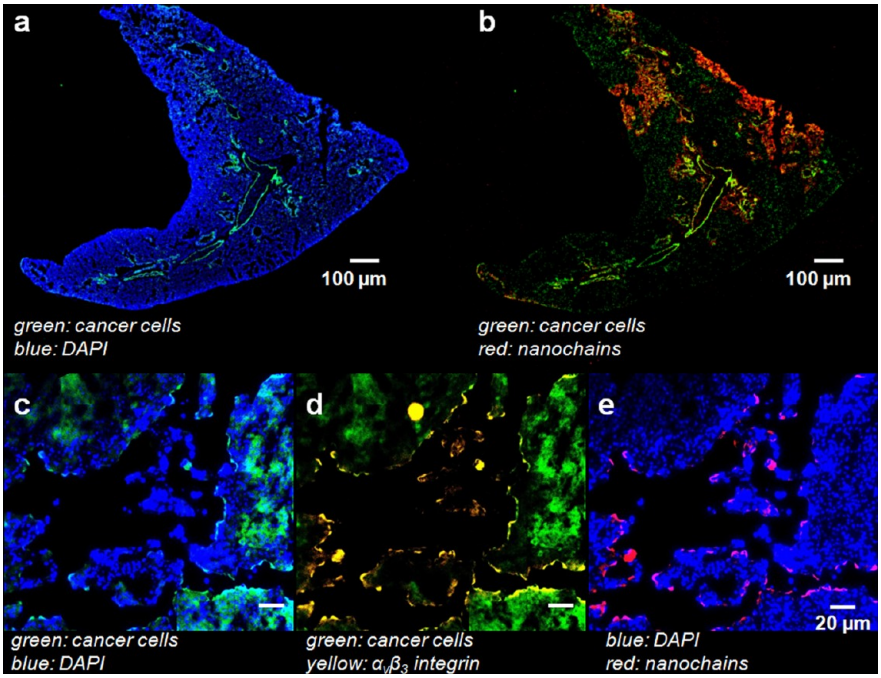

Figure 7. Histological evaluation of the microdistribution of the RGD-NC nanoparticles in the lungs of animal with metastatic tumors. (a,b) Colocalization of fluorescently tagged RGD-NC particles and metastatic cancer cells is shown in the same histological section (5× magnification; green, 4T1 cancer cells; red, RGD-NC; blue, DAPI). (c−e) Location of RGD-NC particles is shown with respect to metastatic cancer cells and expression of $\alpha_v\beta_3$ integrin in the same histological section (40× magnification; blue, DAPI; green, 4T1 cancer cells; yellow, $\alpha v\beta 3$ integrin; red, RGD-NC).

integrin expression was observed in the normal parenchyma of liver (images not shown). The expression of integrins of metastatic cancer cells on the endothelium should favor vascular targeting of the RGD-NC nanoparticles to metastatic tumors. Indeed, fluorescence microscopy showed that RGD-NC particles were predominantly distributed around those same blood vessels colonized by 4T1 cells. Furthermore, the nanoparticles colocalized with the integrin expression of 4T1 cancer cells (Figure 6d−f). In addition to fluorescence microscopy showing the colocalization of cancer cells and RGD-NC particles, bright-field microscopy was performed on the same histological sections after standard hematoxylin−eosin staining (Figure 6g,h).

We also performed histological analysis on the lungs of the same animals. Figure 7a shows that micrometastases were present in the lungs at week 5 after tumor inoculation. Similarly to the liver, the RGD-NC particles accumulated in those locations that were colonized by metastatic cancer cells (Figure 7b). Notably, Figure 7c−e indicates that the location of RGD-NC coincided with overexpression of $\alpha_v\beta_3$ integrins on the metastasized cancer cells.

DISCUSSION

By defining the topology of two different functional groups on the surface of the parent IO nanospheres, we were able to assemble four nanospheres in a linear orientation. Furthermore, the robustness of the nanochain synthesis[25,26] enabled fabricating the chain-shaped nanoparticle with a high degree of uniformity. The effect of shape[43,44] and clustering of iron oxide cores[45,46] significantly increased the T_2 relaxivity per particle compared to their spherical counterparts, which is highly beneficial in imaging of vascular targets.

Another advantage of the nanochain technology is the control of the shape and overall dimensions of the nanoparticle. The *in vitro* flow and *in vivo* FMT imaging studies revealed that the oblate shape of the RGD-NC nanoparticles resulted in superior attachment of the nanochains to the target site compared to spherical nanoparticles. The shape of nanoparticles has been shown to play a critical role in their margination toward the vessel walls in microcirculation.[30,31,47] In contrast to spherical particles, oblate-shaped particles are subjected to torques resulting in tumbling and rotation.[29,30] These complex dynamics of nonspherical particles cause translational as well as rotational motions. In a previous study,[32] we showed that a rod-shaped nanoparticle displayed ∼8 times higher margination rate than a comparable nanosphere. Thus, by defining the geometry of the RGD-NC nanoparticle with an aspect ratio of about 5,[27,48] the particles had an increased ability to sense the overexpression of specific receptors (*i.e.*, β_3 integrins) of the tumor-associated endothelium, which was our "docking site" on metastatic tumors.

In addition to the high probability of the RGD-NC particles to interact with the vascular bed of tumors, the shape of the RGD-NC particles enhanced their

adhesive strength for vascular targeting. In general, while nanoparticles provide enhanced targeting avidity due to multivalent interactions, the geometry of the nanochains further enhanced the ligand−receptor interactions, increasing the likelihood of specific recognition of tumors. Successful vascular targeting requires that the adhesive strength of the nanoparticle offsets the hemodynamic forces applied on the particle tending to detach the particle from the endothelium. In comparison to spherical nanoparticles, oblate-shaped nanoparticles, such as the RGD-NC nanoparticle, form a greater number of ligand−receptor occurrences per particle while the blood-flow-related forces are lower.[27]

Even with their high avidity, one would expect a relatively small number of RGD-NC particles to accumulate at sites of metastasis due to the small size, dispersion, and low degree of neovascularization of metastatic lesions. While tumors larger than 100 mm^3 may favor the EPR effect resulting in deposition of high amounts of nanoparticles in primary tumors, this is not the case for metastatic tumors.[49] For example, liver is one of the most common organs for metastasis of breast cancer.[50,51] Typically, normal liver displays a higher vascular density than liver metastases.[52,53] Post-mortem analysis of histological liver sections from women with metastatic breast cancer revealed that metastatic tumors presented a lower number of vessels than the liver parenchyma.[50] In conjunction with the absence of EPR-driven accumulation of nanoparticles into metastases, it is apparent that successful vascular targeting becomes essential.

Thus, the biological mechanisms of metastasis have to be carefully considered to design metastasis-targeted nanomaterials. During cancer progression, tumor cells show changes in their plasticity, including the epithelial to mesenchymal transition (EMT), which is strongly associated with cell invasion and migration. Numerous factors have been identified to induce EMT including substrate-binding integrins, resulting in a mesenchymal-like cell that is able to move freely by forming focal adhesions.[54−56] Following intravasation, integrin expression on the circulating cancer cells plays a central role in the formation of metastases at a distal site. Extensive experimental evidence also shows that tumor cells interact with platelets supporting tumor metastasis. The β_3 integrin-mediated binding to activated platelets protects tumor cells from the immune system and promotes their arrest at the endothelium, supporting the establishment of metastatic secondary lesions.[10,11] While initial adhesion onto endothelium involves selectins, CD44, and other glycoconjugates, the metastatic site transitions from selectin-dependent tumor cell rolling on the endothelium to firm attachment that is mediated by integrins.[10,12] Not surprisingly, analysis of the adhesiveness of blood-circulating cancer cells revealed that cell attachment to the vasculature requires a key integrin, $\alpha_v\beta_3$.[13−15] Therefore, peptides targeting $\alpha_v\beta_3$ integrin are exceptionally capable ligands to direct the nanochains to locations of metastasis.

Besides primary and metastatic tumors, the $\alpha_v\beta_3$ integrin is expressed in the extracellular matrix since this integrin mediates the adhesion of normal cells to a large number of extracellular matrix proteins, including fibronectin, fibrinogen, collagen, and laminin. However, due to its size, a nanochain cannot extravasate through normal endothelium into normal tissues. More importantly, our strategy depends on vascular targeting with the targeting site being the endothelium of metastasis-associated blood vessels. While $\alpha_v\beta_3$ integrin is minimally expressed on normal resting blood vessels, it is significantly upregulated in the lumen of newly formed blood vessels within primary tumors or blood vessels that have been colonized by metastatic cancer cells.[25,57,58] Thus, besides $\alpha_v\beta_3$ integrin in blood vessels during wound healing,[59] vascular targeting of the RGD-NC particle provides specific binding to metastatic sites.

Indeed, histological evaluation of metastatic tumors showed that clusters of metastatic cancer cells were residing on the endothelium of blood vessels, which coincided with an overexpression of integrins. More importantly, the RGD-NC particles colocalized in exactly these endothelial walls associated with the metastatic cancer cells. Even though the RGD-NC particles exhibited high avidity for integrin-expressing cells, it is very challenging to discriminate the vascular targeting-based signal from the intravascular signal of the agent circulating in the bloodstream of a tumor vessel associated with a metastatic tumor.[39] While prolonged blood circulation of nanoparticles may be desirable in therapeutic scenarios, detection of metastasis will be "masked" since the signal from high levels of circulating nanochains in the bloodstream will "interfere" with the signal from successfully targeted nanochains on the tumor-associated vascular bed. The ideal scenario of a clinically relevant imaging protocol for detection of metastases would require a few hours using an imaging agent with suitable time windows for its targeting and clearance from the bloodstream. Such an imaging agent should sufficiently circulate to effectively target metastatic lesions in a short time frame (*i.e.*, within hours after administration), at which time point its concentration in the blood is low, resulting in the greatest contrast enhancement. Thus, the blood circulation (Figure 2c) and tumor-targeting profiles of the RGD-NC nanoparticles (Figure 2d) satisfy the design criterion for a nanoparticle-based imaging agent.

In particular, imaging metastasis in the liver with targeted nanoparticles presents challenges due to the fact that nanoparticles are cleared by Kupffer cells in the liver, which creates background signal and potential false positive diagnoses. However, the distribution

of cleared nanoparticles is relatively homogeneous in the liver, resulting in homogeneous contrast enhancement without hot spots. Furthermore, the dose of the RGD-NC agent used in this study is relatively low, resulting in low and homogeneous contrast enhancement in the liver due to clearance of the agent. Notably, the metastatic sites appeared as hot spots with significantly higher contrast enhancement than the background signal from the rest of the liver tissue. However, further studies are required to accurately measure the diagnostic sensitivity, specificity, and positive predictive value of this technology.

To date, imaging applications of nanoparticles have focused predominantly on targeting tumors at the primary site (*e.g.*, integrins, folate receptor, EGFR, HER2, *etc.*).[16−24,60−65] Even though attention of the field has recently shifted toward metastasis, there are still very few examples of diagnostics for metastases,[6] including contrast agents for radioimaging of molecular markers (*e.g.*, targeting $\alpha_v\beta_3$ integrins[66,67] or CXCR-4[68]), visualization aids for surgery, and HER2-targeting IO nanoparticles.[69] While the detection accuracy of CT, MRI, and fluorodeoxyglucose positron emission tomography (FDG-PET) for relatively large metastatic tumors (>1 cm in size) has significantly improved in the recent past,[70−72] current imaging methods rarely detect the early spread of metastatic tumor cells,[73] which prohibits early and most likely effective interventions. Treatment decisions of metastatic disease (*e.g.*, surgical resection, radiation, thermal and radio frequency ablation) heavily depends on imaging and diagnostic tools to detect the precise location and extent of disease spread.[74] Micrometastases (0.2−2 mm in size) can rarely be detected *via* changes in perfusion using radionuclide or Doppler perfusion techniques.[75,76] In this work, we show that nanoparticles offer unique opportunities to deal with the complexity of metastatic cancer by exploiting properties that appear at the nanoscale.

CONCLUSION

In conclusion, we demonstrated that the geometry of a chain-shaped nanoparticle promoted targeting of metastatic tumors due to multivalent docking onto integrins of the vascular bed of metastasis. Using multimodal *in vivo* imaging (*i.e.*, FMT and MRI), we were able to image metastatic tumors in the liver and lungs in a highly aggressive breast tumor model. As the biological mechanisms of metastasis continue to unravel, we expect that more surface markers of metastatic lesions will be identified that can be employed by nanoparticle delivery systems for targeting metastatic disease.

METHODS

Synthesis and Characterization of the Nanochain Particles. The nanochains were synthesized following our previously published method.[26] Briefly, solid-phase chemistry was used to partially modify the surface functionality of IO nanospheres. CLEAR resin (Peptides International Inc., Louisville, KY) functionalized with amines was modified with a homobifunctional cleavable cross-linker reactive toward amines (DTSSP). Amine-functionalized IO nanospheres were introduced, allowed to bind to the solid support, and then cleaved off using a reducing agent (TCEP). The same type of resin was used, and the modified spheres with surface asymmetry were introduced in a step-by-step manner. After recovering the chain *via* a reducing agent, the suspension was further cleaned using dialysis. The nanoparticles were characterized in terms of their size (DLS), structure (TEM), and magnetic relaxivity (Bruker minispec relaxometer). The cyclo (Arg-Gly-Asp-D-Phe-Cys) or c(RGDfC) was conjugated onto PEG(3400) *via* maleimide chemistry. In addition to conjugation of the cRGDe peptide, the nanochain particles were tagged with an NIR fluorophore (Vivotag 680) to be detectable by FMT imaging or fluorescence spectroscopy or microscopy. Details of the synthesis and characterization of the nanoparticles are shown in the Supporting Information.

Mouse Tumor Model. All animal procedures were conducted under a protocol approved by the CWRU IACUC. We used an orthotopic 4T1 breast tumor model in mice.[77] The 4T1 cell line was engineered to stably express green fluorescent protein (GFP) to allow tracking and quantification of the cells *in vivo* and histologically. Briefly, we inoculated 0.5×10^6 4T1 cells orthotopically in a no. 9 mammary fat pad of female BALB/c mice that was surgically exposed while the mice were anesthetized. The animals were used in the *in vivo* studies at week 2 (only primary tumor) or week 5 (primary and metastatic tumors). On the basis of our prior experience, we chose these time points because they represent different stages of angiogenesis, necrosis, invasion, and metastasis and are informative and relevant to the human disease.

Fluorescence Molecular Tomography. We performed fluorescence imaging on the 4T1 mammary model in mice (at week 2 or 5) using the FMT 2500 quantitative yomography *in vivo* imaging system (Perkin-Elmer). Phantoms for each nanoparticle formulation were used to calibrate the FMT to take quantitative deposition measurements. We then intravenously injected each of the four formulations at a dose of 1.3×10^{14} particles per kg b.w. The animals were imaged before and after IV injection of the formulations at multiple time points (15, 30, 45 min and 3, 6, 24 h). After the last imaging session, tumor and organs (kidneys, lungs, brain, liver, spleen, and intestine) were retrieved and weighed. To verify the findings of the *in vivo* imaging and confirm the presence of metastases in the organs, we imaged the organs *ex vivo* using the FMT and a CRi Maestro fluorescence imaging system. The organs were then processed for histological analysis.

Angiography Using Contrast-Enhanced Micro-CT Imaging. Contrast-enhanced angiography was performed using a Siemens Inveon micro-CT system (isotropic 99 μm resolution, 80 kVp, 500 μA) and a long-circulating liposomal imaging agent encapsulating a high cargo of an iodinated contrast agent.[39] Following IV injection of the agent at a dose of 2.6 g iodine/kg b.w., the animals were imaged with the micro-CT system. Subsequently, the animals were IV-injected with RGD-NC followed by imaging with the FMT system. The two images were co-registered using a semiautomatic 3D segmentation-based registration approach that was implemented in script-based software (in MATLAB) and interactive visualization software Amira (Visage Imaging Inc.).[78] Fiducial markers placed around the tumor mass were visible in both the micro-CT and the FMT images. Using a region growing algorithm with seed points defined by the user, we segmented the fiducial markers from both volumes.[79] Then, we used Amira's AffineTransform tool to register the floating volume landmarks to the reference volume landmarks.

MR Imaging. MR images were acquired on a 9.4 T Bruker MRI system. A volume coil (3.5 cm inner diameter) was employed.

High-resolution images were obtained before and 15, 30, 45, 60, and 120 min after IV injection of the RGD-NC nanoparticles (at a dose of 7.5 mg Fe/kg b.w.) using a T_2-weighted RARE sequence with the following parameters: TR/TE = 1000/45 ms, matrix = 128 × 128, FOV = 5 × 5 cm, and 1 average. This resulted in an in-plane spatial resolution of 390 μm and a slice thickness of 1 mm.

Histological Evaluation. After the last imaging acquisition with FMT or MRI, tissues were collected from the mice for histological studies. The animals were anesthetized with an IP injection of ketamine/xylazine and transcardially perfused with heparinized PBS followed by 4% paraformaldehyde in PBS. Tumors and organs were explanted and postfixed overnight in 4% paraformaldehyde in PBS. The tissues were soaked in 30% sucrose (w/v) in PBS at 4 °C for cryosectioning. Serial sections of 12 μm thickness were collected using a cryostat (Leica CM 300). To visualize the tumor microvasculature, the tissue slices were immunohistochemically stained for the endothelial antigen CD31 (BD Biosciences, Pharmingen). The tissues were also stained with the nuclear stain DAPI. Standard hematoxylin–eosin staining was also performed. The tissue sections were imaged at 5, 10, or 40× on the Zeiss Axio Observer Z1 motorized FL inverted microscope. To obtain an image of the entire tissue section, a montage of each section was made using the automated tiling function of the microscope.

Statistical Analysis. Means were determined for each variable in this study, and the resulting values from each experiment were subjected to one-way analysis of variance with post-hoc Bonferroni test. A P value of less than 0.01 was used to confirm significant differences. Normality of each data set was confirmed using the Anderson–Darling test.

Conflict of Interest: The authors declare no competing financial interest.

Acknowledgment. This work was partially supported by a grant from the American Cancer Society IRG-91-022-18 (E.K.) and a pilot grant from the Case Comprehensive Cancer Center P30 CA043703 (E.K.). R.T. was supported by a fellowship from the NIH Interdisciplinary Biomedical Imaging Training Program (5T32EB007509). Z.B. was supported by a fellowship from the NIH Medical Student Research Training grant (T35HL082544). We thank Dr. James Basilion for discussions, and Erik Schmidt, Christopher Shoup. and A. Lee Rivera for help with the particle fabrication and the *in vitro* flow experiments. We also thank Kristen Lozada, Joseph Meyers, Gopal Ramamurthy, and Tenia Harris for help with the animal studies.

Supporting Information Available: Additional figures and experimental details. This material is available free of charge *via* the Internet at http://pubs.acs.org.

REFERENCES AND NOTES

1. Maeda, H.; Wu, J.; Sawa, T.; Matsumura, Y.; Hori, K. Tumor Vascular Permeability and the EPR Effect in Macromolecular Therapeutics: A Review. *J. Controlled Release* **2000**, *65*, 271–284.
2. Gradishar, W. J.; Tjulandin, S.; Davidson, N.; Shaw, H.; Desai, N.; Bhar, P.; Hawkins, M.; O'Shaughnessy, J. Phase III Trial of Nanoparticle Albumin-Bound Paclitaxel Compared with Polyethylated Castor Oil-Based Paclitaxel in Women with Breast Cancer. *J. Clin. Oncol.* **2005**, *23*, 7794–7803.
3. Lasic, D. D. Doxorubicin in Sterically Stabilized Liposomes. *Nature* **1996**, *380*, 561–562.
4. Lasic, D. D.; Papahadjopoulos, D. Liposomes Revisited. *Science* **1995**, *267*, 1275–1276.
5. Safra, T. Cardiac Safety of Liposomal Anthracyclines. *Oncologist* **2003**, *8*, 17–24.
6. Schroeder, A.; Heller, D. A.; Winslow, M. M.; Dahlman, J. E.; Pratt, G. W.; Langer, R.; Jacks, T.; Anderson, D. G. Treating Metastatic Cancer with Nanotechnology. *Nat. Rev. Cancer* **2012**, *12*, 39–50.
7. *Cancer Facts and Figures 2011*; American Cancer Society, 2011.
8. van Zijl, F.; Krupitza, G.; Mikulits, W. Initial Steps of Metastasis: Cell Invasion and Endothelial Transmigration. *Mutat. Res.* **2011**, *728*, 23–34.
9. Coghlin, C.; Murray, G. I. Current and Emerging Concepts in Tumour Metastasis. *J. Pathol.* **2010**, *222*, 1–15.
10. Gay, L. J.; Felding-Habermann, B. Contribution of Platelets to Tumour Metastasis. *Nat. Rev. Cancer* **2011**, *11*, 123–134.
11. Felding-Habermann, B.; Habermann, R.; Saldivar, E.; Ruggeri, Z. M. Role of β_3 Integrins in Melanoma Cell Adhesion to Activated Platelets under Flow. *J. Biol. Chem.* **1996**, *271*, 5892–5900.
12. McCarty, O. J.; Mousa, S. A.; Bray, P. F.; Konstantopoulos, K. Immobilized Platelets Support Human Colon Carcinoma Cell Tethering, Rolling, and Firm Adhesion under Dynamic Flow Conditions. *Blood* **2000**, *96*, 1789–1797.
13. Arnaout, M. A.; Mahalingam, B.; Xiong, J. P. Integrin Structure, Allostery, and Bidirectional Signaling. *Annu. Rev. Cell Dev. Biol.* **2005**, *21*, 381–410.
14. Felding-Habermann, B.; O'Toole, T. E.; Smith, J. W.; Fransvea, E.; Ruggeri, Z. M.; Ginsberg, M. H.; Hughes, P. E.; Pampori, N.; Shattil, S. J.; Saven, A.; *et al.* Integrin Activation Controls Metastasis in Human Breast Cancer. *Proc. Natl. Acad. Sci. U.S.A.* **2001**, *98*, 1853–1858.
15. Lorger, M.; Krueger, J. S.; O'Neal, M.; Staflin, K.; Felding-Habermann, B. Activation of Tumor Cell Integrin $\alpha_v\beta_3$ Controls Angiogenesis and Metastatic Growth in the Brain. *Proc. Natl. Acad. Sci. U.S.A.* **2009**, *106*, 10666–10671.
16. Desgrosellier, J. S.; Cheresh, D. A. Integrins in Cancer: Biological Implications and Therapeutic Opportunities. *Nat. Rev. Cancer* **2010**, *10*, 9–22.
17. Chen, K.; Chen, X. Integrin Targeted Delivery of Chemotherapeutics. *Theranostics* **2011**, *1*, 189–200.
18. Huang, G.; Zhou, Z.; Srinivasan, R.; Penn, M. S.; Kottke-Marchant, K.; Marchant, R. E.; Gupta, A. S. Affinity Manipulation of Surface-Conjugated RGD Peptide To Modulate Binding of Liposomes to Activated Platelets. *Biomaterials* **2008**, *29*, 1676–1685.
19. Zhang, C.; Jugold, M.; Woenne, E. C.; Lammers, T.; Morgenstern, B.; Mueller, M. M.; Zentgraf, H.; Bock, M.; Eisenhut, M.; Semmler, W.; *et al.* Specific Targeting of Tumor Angiogenesis by RGD-Conjugated Ultrasmall Superparamagnetic Iron Oxide Particles Using a Clinical 1.5-T Magnetic Resonance Scanner. *Cancer Res.* **2007**, *67*, 1555–1562.
20. Ke, T.; Jeong, E. K.; Wang, X.; Feng, Y.; Parker, D. L.; Lu, Z. R. RGD Targeted Poly(L-glutamic acid)-Cystamine-(Gd-Do3a) Conjugate for Detecting Angiogenesis Biomarker $\alpha_v\beta_3$ Integrin with Mrt, Mapping. *Int. J. Nanomed.* **2007**, *2*, 191–199.
21. Danhier, F.; Vroman, B.; Lecouturier, N.; Crokart, N.; Pourcelle, V.; Freichels, H.; Jerome, C.; Marchand-Brynaert, J.; Feron, O.; Preat, V. Targeting of Tumor Endothelium by RGD-Grafted PLGA-Nanoparticles Loaded with Paclitaxel. *J. Controlled Release* **2009**, *140*, 166–173.
22. Montet, X.; Funovics, M.; Montet-Abou, K.; Weissleder, R.; Josephson, L. Multivalent Effects of RGD Peptides Obtained by Nanoparticle Display. *J. Med. Chem.* **2006**, *49*, 6087–6093.
23. Liu, X. Q.; Song, W. J.; Sun, T. M.; Zhang, P. Z.; Wang, J. Targeted Delivery of Antisense Inhibitor of MiRNA for Antiangiogenesis Therapy Using cRGD-Functionalized Nanoparticles. *Mol. Pharmaceutics* **2011**, *8*, 250–259.
24. Murphy, E. A.; Majeti, B. K.; Barnes, L. A.; Makale, M.; Weis, S. M.; Lutu-Fuga, K.; Wrasidlo, W.; Cheresh, D. A. Nanoparticle-Mediated Drug Delivery to Tumor Vasculature Suppresses Metastasis. *Proc. Natl. Acad. Sci. U.S.A.* **2008**, *105*, 9343–9348.
25. Peiris, P. M.; Bauer, L.; Toy, R.; Tran, E.; Pansky, J.; Doolittle, E.; Schmidt, E.; Hayden, E.; Mayer, A.; Keri, R. A.; *et al.* Enhanced Delivery of Chemotherapy to Tumors Using a Multicomponent Nanochain with Radio-Frequency-Tunable Drug Release. *ACS Nano* **2012**, *6*, 4157–4168.
26. Peiris, P. M.; Schmidt, E.; Calabrese, M.; Karathanasis, E. Assembly of Linear Nano-Chains from Iron Oxide Nanospheres with Asymmetric Surface Chemistry. *PLoS One* **2011**, *6*, e15927.
27. Decuzzi, P.; Ferrari, M. The Adhesive Strength of Non-spherical Particles Mediated by Specific Interactions. *Biomaterials* **2006**, *27*, 5307–5314.

28. Gao, B.; Saba, T. M.; Tsan, M. F. Role of $\alpha_v\beta_3$-Integrin in TNF-α-Induced Endothelial Cell Migration. *Am. J. Physiol. Cell Physiol.* **2002**, *283*, C1196–C1205.
29. Gavze, E.; Shapiro, M. Motion of Inertial Spheroidal Particles in a Shear Flow near a Solid Wall with Special Application to Aerosol Transport in Microgravity. *J. Fluid Mech.* **1998**, *371*, 59–79.
30. Lee, S. Y.; Ferrari, M.; Decuzzi, P. Shaping Nano-/Micro-Particles for Enhanced Vascular Interaction in Laminar Flows. *Nanotechnology* **2009**, *20*, 495101.
31. Gentile, F.; Chiappini, C.; Fine, D.; Bhavane, R. C.; Peluccio, M. S.; Cheng, M. M.; Liu, X.; Ferrari, M.; Decuzzi, P. The Effect of Shape on the Margination Dynamics of Non-neutrally Buoyant Particles in Two-Dimensional Shear Flows. *J. Biomech.* **2008**, *41*, 2312–2318.
32. Toy, R.; Hayden, E.; Shoup, C.; Baskaran, H.; Karathanasis, E. The Effects of Particle Size, Density and Shape on Margination of Nanoparticles in Microcirculation. *Nanotechnology* **2011**, *22*, 115101.
33. Ganong, W. F. *Review of Medical Physiology*, 21st ed.; Lange Medical Books/McGraw-Hill, Medical Publishing Division: New York, 2003.
34. Tao, K.; Fang, M.; Alroy, J.; Sahagian, G. G. Imagable 4T1 Model for the Study of Late Stage Breast Cancer. *BMC Cancer* **2008**, *8*, 228.
35. Dykxhoorn, D. M.; Wu, Y.; Xie, H.; Yu, F.; Lal, A.; Petrocca, F.; Martinvalet, D.; Song, E.; Lim, B.; Lieberman, J. Mir-200 Enhances Mouse Breast Cancer Cell Colonization To Form Distant Metastases. *PLoS One* **2009**, *4*, e7181.
36. McNeeley, K. M.; Karathanasis, E.; Annapragada, A. V.; Bellamkonda, R. V. Masking and Triggered Unmasking of Targeting Ligands on Nanocarriers To Improve Drug Delivery to Brain Tumors. *Biomaterials* **2009**, *30*, 3986–3995.
37. McNeeley, K. M.; Annapragada, A.; Bellamkonda, R. V. Decreased Circulation Time Offsets Increased Efficacy of PEGylated Nanocarriers Targeting Folate Receptors of Glioma. *Nanotechnology* **2007**, *18*, 385101.
38. Karathanasis, E.; Chan, L.; Balusu, S. R.; D'Orsi, C. J.; Annapragada, A. V.; Sechopoulos, I.; Bellamkonda, R. V. Multifunctional Nanocarriers for Mammographic Quantification of Tumor Dosing and Prognosis of Breast Cancer Therapy. *Biomaterials* **2008**, *29*, 4815–4822.
39. Karathanasis, E.; Suryanarayanan, S.; Balusu, S. R.; McNeeley, K.; Sechopoulos, I.; Karellas, A.; Annapragada, A. V.; Bellamkonda, R. V. Imaging Nanoprobe for Prediction of Outcome of Nanoparticle Chemotherapy by Using Mammography. *Radiology* **2009**, *250*, 398–406.
40. Karathanasis, E.; Chan, L.; Karumbaiah, L.; McNeeley, K.; D'Orsi, C. J.; Annapragada, A. V.; Sechopoulos, I.; Bellamkonda, R. V. Tumor Vascular Permeability to a Nanoprobe Correlates to Tumor-Specific Expression Levels of Angiogenic Markers. *PLoS ONE* **2009**, *4*, e5843.
41. Vasquez, K. O.; Casavant, C.; Peterson, J. D. Quantitative Whole Body Biodistribution of Fluorescent-Labeled Agents by Non-invasive Tomographic Imaging. *PLoS One* **2011**, *6*, e20594.
42. Crayton, S. H.; Tsourkas, A. pH-Titratable Superparamagnetic Iron Oxide for Improved Nanoparticle Accumulation in Acidic Tumor Microenvironments. *ACS Nano* **2011**, *5*, 9592–9601.
43. Park, J. H.; von Maltzahn, G.; Zhang, L. L.; Schwartz, M. P.; Ruoslahti, E.; Bhatia, S. N.; Sailor, M. J. Magnetic Iron Oxide Nanoworms for Tumor Targeting and Imaging. *Adv. Mater.* **2008**, *20*, 1630–1635.
44. Gossuin, Y.; Disch, S.; Vuong, Q. L.; Gillis, P.; Hermann, R. P.; Park, J. H.; Sailor, M. J. NMR Relaxation and Magnetic Properties of Superparamagnetic Nanoworms. *Contrast Media Mol. Imaging* **2010**, 10.1002/cmmi.387.
45. Lu, J.; Ma, S.; Sun, J.; Xia, C.; Liu, C.; Wang, Z.; Zhao, X.; Gao, F.; Gong, Q.; Song, B.; *et al.* Manganese Ferrite Nanoparticle Micellar Nanocomposites as MRI Contrast Agent for Liver Imaging. *Biomaterials* **2009**, *30*, 2919–2928.
46. Ai, H.; Flask, C.; Weinberg, B.; Shuai, X.; Pagel, M. D.; Farrel, D.; Duerk, J.; Gao, J. Magnetite-Loaded Polymeric Micelles as Ultrasensitive Magnetic-Resonance Probes. *Adv. Mater.* **2005**, *17*, 1949–1952.
47. Chauhan, V. P.; Popovic, Z.; Chen, O.; Cui, J.; Fukumura, D.; Bawendi, M. G.; Jain, R. K. Fluorescent Nanorods and Nanospheres for Real-Time *In Vivo* Probing of Nanoparticle Shape-Dependent Tumor Penetration. *Angew. Chem., Int. Ed.* **2011**, *50*, 11417–11420.
48. Decuzzi, P.; Causa, F.; Ferrari, M.; Netti, P. A. The Effective Dispersion of Nanovectors within the Tumor Microvasculature. *Annu. Rev. Biomed. Eng.* **2006**, *34*, 633–641.
49. Adiseshaiah, P. P.; Hall, J. B.; McNeil, S. E. Nanomaterial Standards for Efficacy and Toxicity Assessment. *Wiley Interdiscip. Rev. Nanomed. Nanobiotechnol.* **2010**, *2*, 99–112.
50. Nacev, A.; Kim, S. H.; Rodriguez-Canales, J.; Tangrea, M. A.; Shapiro, B.; Emmert-Buck, M. R. A Dynamic Magnetic Shift Method To Increase Nanoparticle Concentration in Cancer Metastases: A Feasibility Study Using Simulations on Autopsy Specimens. *Int. J. Nanomed.* **2011**, *6*, 2907–2923.
51. Pagani, O.; Senkus, E.; Wood, W.; Colleoni, M.; Cufer, T.; Kyriakides, S.; Costa, A.; Winer, E. P.; Cardoso, F. International Guidelines for Management of Metastatic Breast Cancer: Can Metastatic Breast Cancer Be Cured? *J. Natl. Cancer Inst.* **2010**, *102*, 456–463.
52. Kennecke, H.; Yerushalmi, R.; Woods, R.; Cheang, M. C.; Voduc, D.; Speers, C. H.; Nielsen, T. O.; Gelmon, K. Metastatic Behavior of Breast Cancer Subtypes. *J. Clin. Oncol.* **2010**, *28*, 3271–3277.
53. Terayama, N.; Terada, T.; Nakanuma, Y. An Immunohistochemical Study of Tumour Vessels in Metastatic Liver Cancers and the Surrounding Liver Tissue. *Histopathology* **1996**, *29*, 37–43.
54. Friedl, P.; Gilmour, D. Collective Cell Migration in Morphogenesis, Regeneration and Cancer. *Nat. Rev. Mol. Cell Biol.* **2009**, *10*, 445–457.
55. Bidard, F. C.; Pierga, J. Y.; Vincent-Salomon, A.; Poupon, M. F. A "Class Action" Against the Microenvironment: Do Cancer Cells Cooperate in Metastasis? *Cancer Metastasis Rev.* **2008**, *27*, 5–10.
56. Kirfel, G.; Rigort, A.; Borm, B.; Herzog, V. Cell Migration: Mechanisms of Rear Detachment and the Formation of Migration Tracks. *Eur. J. Cell. Biol.* **2004**, *83*, 717–724.
57. Brooks, P. C.; Clark, R. A.; Cheresh, D. A. Requirement of Vascular Integrin $\alpha_v\beta_3$ for Angiogenesis. *Science* **1994**, *264*, 569–571.
58. Brooks, P. C.; Stromblad, S.; Klemke, R.; Visscher, D.; Sarkar, F. H.; Cheresh, D. A. Antiintegrin $\alpha_v\beta_3$ Blocks Human Breast Cancer Growth and Angiogenesis in Human Skin. *J. Clin. Invest.* **1995**, *96*, 1815–1822.
59. Clark, R. A.; Tonnesen, M. G.; Gailit, J.; Cheresh, D. A. Transient Functional Expression of $\alpha_v\beta_3$ on Vascular Cells during Wound Repair. *Am. J. Pathol.* **1996**, *148*, 1407–1421.
60. Huang, X.; Peng, X.; Wang, Y.; Shin, D. M.; El-Sayed, M. A.; Nie, S. A Reexamination of Active and Passive Tumor Targeting by Using Rod-Shaped Gold Nanocrystals and Covalently Conjugated Peptide Ligands. *ACS Nano* **2010**, *4*, 5887–5896.
61. Cheng, Y.; Meyers, J. D.; Agnes, R. S.; Doane, T. L.; Kenney, M. E.; Broome, A. M.; Burda, C.; Basilion, J. P. Addressing Brain Tumors with Targeted Gold Nanoparticles: A New Gold Standard for Hydrophobic Drug Delivery? *Small* **2011**, *7*, 2301–2306.
62. Gabizon, A.; Horowitz, A. T.; Goren, D.; Tzemach, D.; Shmeeda, H.; Zalipsky, S. *In Vivo* Fate of Folate-Targeted Polyethylene-Glycol Liposomes in Tumor-Bearing Mice. *Clin. Cancer Res.* **2003**, *9*, 6551–6559.
63. Gabizon, A.; Shmeeda, H.; Horowitz, A. T.; Zalipsky, S. Tumor Cell Targeting of Liposome-Entrapped Drugs with Phospholipid-Anchored Folic Acid-PEG Conjugates. *Adv. Drug Delivery Rev.* **2004**, *56*, 1177–1192.
64. Park, J. W.; Hong, K.; Kirpotin, D. B.; Colbern, G.; Shalaby, R.; Baselga, J.; Shao, Y.; Nielsen, U. B.; Marks, J. D.; Moore, D.; *et al.* Anti-HER2 Immunoliposomes: Enhanced Efficacy Attributable to Targeted Delivery. *Clin. Cancer Res.* **2002**, *8*, 1172–1181.

65. Park, J. W.; Kirpotin, D. B.; Hong, K.; Shalaby, R.; Shao, Y.; Nielsen, U. B.; Marks, J. D.; Papahadjopoulos, D.; Benz, C. C. Tumor Targeting Using Anti-HER2 Immunoliposomes. *J. Controlled Release* **2001**, *74*, 95–113.
66. Haubner, R.; Wester, H. J.; Weber, W. A.; Mang, C.; Ziegler, S. I.; Goodman, S. L.; Senekowitsch-Schmidtke, R.; Kessler, H.; Schwaiger, M. Noninvasive Imaging of $\alpha_v\beta_3$ Integrin Expression Using 18f-Labeled RGD-Containing Glycopeptide and Positron Emission Tomography. *Cancer Res.* **2001**, *61*, 1781–1785.
67. Haubner, R.; Wester, H. J.; Burkhart, F.; Senekowitsch-Schmidtke, R.; Weber, W.; Goodman, S. L.; Kessler, H.; Schwaiger, M. Glycosylated RGD-Containing Peptides: Tracer for Tumor Targeting and Angiogenesis Imaging with Improved Biokinetics. *J. Nucl. Med.* **2001**, *42*, 326–336.
68. Nimmagadda, S.; Pullambhatla, M.; Stone, K.; Green, G.; Bhujwalla, Z. M.; Pomper, M. G. Molecular Imaging of Cxcr4 Receptor Expression in Human Cancer Xenografts with [64Cu]AMD3100 Positron Emission Tomography. *Cancer Res.* **2010**, *70*, 3935–3944.
69. Kievit, F. M.; Stephen, Z. R.; Veiseh, O.; Arami, H.; Wang, T.; Lai, V. P.; Park, J. O.; Ellenbogen, R. G.; Disis, M. L.; Zhang, M. Targeting of Primary Breast Cancers and Metastases in a Transgenic Mouse Model Using Rationally Designed Multifunctional SPIONs. *ACS Nano* **2012**, *6*, 2591–2601.
70. Kinkel, K.; Lu, Y.; Both, M.; Warren, R. S.; Thoeni, R. F. Detection of Hepatic Metastases from Cancers of the Gastrointestinal Tract by Using Noninvasive Imaging Methods (US, CT, MR Imaging, PET): A Meta-Analysis. *Radiology* **2002**, *224*, 748–756.
71. Bipat, S.; van Leeuwen, M. S.; Comans, E. F.; Pijl, M. E.; Bossuyt, P. M.; Zwinderman, A. H.; Stoker, J. Colorectal Liver Metastases: CT, MR Imaging, and PET for Diagnosis—Meta-Analysis. *Radiology* **2005**, *237*, 123–131.
72. Niekel, M. C.; Bipat, S.; Stoker, J. Diagnostic Imaging of Colorectal Liver Metastases with CT, MR Imaging, FDG PET, and/or FDG PET/CT: A Meta-Analysis of Prospective Studies Including Patients Who Have Not Previously Undergone Treatment. *Radiology* **2011**, *257*, 674–684.
73. Pantel, K.; Alix-Panabieres, C.; Riethdorf, S. Cancer Micrometastases. *Nat. Rev. Clin. Oncol.* **2009**, *6*, 339–351.
74. Robinson, P. J. The Early Detection of Liver Metastases. *Cancer Imaging* **2002**, *2*, 1–3.
75. Huvos, A. G.; Hutter, R. V.; Berg, J. W. Significance of Axillary Macrometastases and Micrometastases in Mammary Cancer. *Ann. Surg.* **1971**, *173*, 44–46.
76. Rampaul, R. S.; Miremadi, A.; Pinder, S. E.; Lee, A.; Ellis, I. O. Pathological Validation and Significance of Micrometastasis in Sentinel Nodes in Primary Breast Cancer. *Breast Cancer Res.* **2001**, *3*, 113–116.
77. Yori, J. L.; Seachrist, D. D.; Johnson, E.; Lozada, K. L.; Abdul-Karim, F. W.; Chodosh, L. A.; Schiemann, W. P.; Keri, R. A. Kruppel-like Factor 4 Inhibits Tumorigenic Progression and Metastasis in a Mouse Model of Breast Cancer. *Neoplasia* **2011**, *13*, 601–610.
78. Maintz, J. B. A.; Viergever, M. A. A Survey of Medical Image Registration. *Med. Image Anal.* **1998**, *2*, 1–36.
79. Gonzalez, R. C., Woods, R.E. *Digital Image Processing*, 2nd ed.; Prentice Hall: New York, 2002.